Journal of Fluorine Chemistry 132 (2011) 651–659

Contents lists available at ScienceDirect

Journal of Fluorine Chemistry

journal homepage: www.elsevier.com/locate/fluor

Structural architecture and physical properties of some inorganic fluoride series: a review

Alain Tressaud

Institute of Condensed Matter Chemistry of Bordeaux (ICMCB-CNRS), Université Bordeaux, 87 Ave Dr. A Schweitzer, 33608 Pessac, France

ARTICLE INFO

Article history:
Received 14 March 2011
Received in revised form 11 May 2011
Accepted 13 May 2011
Available online 20 May 2011

Keywords:
Metal fluorides
Perovskite
Fluorination
ReO_3
Elpasolite
HTB
Pyrochlore
Ferromagnetism
Piezoconductivity
Ferroelasticity
Surface functionalization
Nano-
Brønsted acidic sites
Lewis acidic sites
Hydroxyl-fluorides

ABSTRACT

Many structural networks of transition metal fluorides and oxide fluorides may be derived from simple units of octahedral MF_6 units, connected by common corners, generally in a 3D way: e.g., perovskite, ReO_3, elpasolite, HTB, TTB, pyrochlore, etc. The accurate knowledge of these structures, together with the stabilities of these phases vs. temperature, allows deeper interpretation and fitting of many of their physical properties. Among the numerous fluoro-compounds which derive from these structural arrangements, several fluorinated and oxyfluorinated series have been chosen to illustrate the great range of outstanding physical properties, including ferromagnetism, piezoconductivity, ferroelasticity, high T_C superconductivity, surface functionalization, that can be better understood with the help of structural considerations. The concept of nanometric particles in materials science has also drastically changed the investigations in solid state fluorine chemistry, not only for finding original synthetic routes, but also new characterization tools. As an example, in nanostructured $M(OH,F)_3$ metal hydroxyfluorides that can be used as acidic heterogeneous catalysts, the morphological nature and specific area of the materials can be tuned by changing the experimental parameters of synthesis. In particular, the number and strength of Brønsted/Lewis acidic sites and the thermal stability can be correlated to the structural arrangements.

1. Introduction

Because of the similar ionic radii of O^{2-} and F^- anions, fluoride and oxide networks often exhibit common structural features deriving from similar anionic packing [1]. However, due to much stronger ionic bonding occurring in fluoride series, drastic differences occur in some of their physical properties; in particular the transport properties of fluorides are influenced by their strong electron localization. On the other hand, due to the straightforward reactivity of fluorine and fluorinated media, the properties of most materials could be easily modulated by surface treatments involving either fluorinated gases or plasmas [2]. For instance, direct F_2-gas or radio-frequency (rf) plasma fluorination allows one to modify drastically at low temperatures the surfaces of various types of materials, including metals, powders, oxide ceramics [3], silica and silicates [4,5], carbons [6], elastomers and polymers [7], etc. This paper will not deal with this aspect of surface fluorine chemistry neither with the powerful possibility to change conduction properties by intercalation of fluorine/fluoride species in graphite and carbon materials, i.e. changing semi-conducting starting graphite to metallic materials [8] and in rare earth cuprates, i.e. creating new high T_C superconductors [9]. The aim of the present paper is rather to elucidate correlations existing between structural characteristics, morphology and physical properties in inorganic solid state fluorides. The three series that have been selected for such a purpose have been chosen to illustrate the great diversity of physical behaviour among metal fluorides and oxide fluorides. These examples have been taken from various solid state fluoro-compounds investigated within the "Bordeaux Fluorine group" over the last several decades.

2. Experimental methods

2.1. Synthesis routes

A large variety of synthetic routes have been designed and developed at ICMCB-CNRS, first by J. Grannec and L. Lozano followed by E. Durand, in order to obtain various types of inorganic

---

E-mail address: tressaud@icmcb-bordeaux.cnrs.fr.

0022-1139/$ – see front matter © 2011 Elsevier B.V. All rights reserved.
doi:10.1016/j.jfluchem.2011.05.014

fluoro-compounds, ranging from large single crystals to nanosized powders with high surface areas (HSA) [10,11].

In the following two main types of synthesis were presented:

- conventional solid state reactions between the starting compounds mixed in stoichiometric amounts. Generally these reactions took place in sealed gold or platinum tubes at high temperature (between 300 and 800 °C, depending on the stabilities and volatilities of the starting materials)
- In order to obtain nanosized HSA particles, in the case of $Al(OH, F)_3$ hydroxyfluorides, the microwave hydrofluorothermal process was used. However, it should be noted that it was often necessary to combine these routes with other types of processing, such as F_2-gas direct fluorination, to obtain the final product in high purity.

Pd_2F_6 was prepared by direct fluorination of palladium sponge. Several 8 hr fluorinations (pressure 1 atm.) at 500 °C were necessary to obtain Pd_2F_6 free of PdF_2 (checked by X-ray diffraction). Between the fluorination cycles, the material was ground in a glove box containing less than 2 ppm H_2O and O_2.

$Pd^{II}Pt^{IV}F_6$: Solid state synthesis from stoichiometric mixtures of PdF_2 and PtF_4 were carried out in sealed platinum tubes at 500 °C. PtF_4 was obtained according to the reaction $4PtF_5 + Pt \rightarrow 5PtF_4$ in sealed platinum tubes at 400 °C under N_2.

$Ni^{II}Pd^{IV}F_6$ and $Ni^{II}Pt^{IV}F_6$ were synthesized in sealed platinum tubes by solid state reaction between NiF_2 and PdF_4 or PtF_4. The reactions were carried out in the 400–600 °C temperature range depending on the compound to be prepared. The final materials were characterized by X-ray diffraction.

$Pt^{II}Pt^{IV}F_6$ was synthesized by selective direct fluorination of Pt sponge at temperatures below 450 °C.

A_2BMX_6 elpasolites (A, B = alkaline cation, $(NH_4)^+$; M = trivalent cation including rare earth elements, X = O, F) were synthesized via solid state reaction at 700 °C in a platinum tube sealed under inert atmosphere. Stoichiometric mixtures of binary fluorides (or oxide fluorides) were used. Because of the high reactivity of fluorides with moist air, strict preparative conditions were employed: dehydration process of monovalent fluorides purification of metal trifluorides under fluorinating atmosphere, grinding in glove box under dry Ar atmosphere. Structural characterizations of final elpasolite compounds were performed using X-ray powder diffractometry, the sample being contained in an air-tight cell with a mylar window.

$Al(OH,F)_3$ nanosized aluminium hydroxyfluorides were synthesized by solvothermal (or hydrofluorothermal) processes, using a MARS-5 Microwave Digestion System (CEM Corp.). Internal pressure and temperature were measured by sensors. In a first step, a precursor solution was prepared as follows: the Al(III) precursor was dissolved in water + solvent solution. An aqueous solution of HF was then added in order to obtain appropriate [HF]/[Al] molar ratio which led to the precipitation of the expected final nano-fluoride. The mixture was placed in a closed Teflon container for microwave hydrothermal synthesis (XP-1500 plus model). Two steps took place during this process. First, the solution was heated at 100 °C (at 288 K/min) for 10 min and then at the synthesis temperature for 30 min for several hours. The very first step was required because of the occurrence of a side reaction induced by microwave irradiation: an exothermic phenomenon leading to an increase in the temperature to 150 °C and an internal pressure reaching about 16–18 bar, takes place after 5 min of irradiation. After the hydrosolvothermal reaction, a microwave-assisted drying was performed under a primary vacuum and argon flow at 100 °C. The powder was then washed with a large amount of ethanol under nitrogen pressure and finally outgassed at 200 °C under vacuum. The effects of these various experimental parameters will be detailed further in Section 5.

2.2. Physical chemical characterizations

2.2.1. X-ray diffraction analysis

Powder diffraction patterns were recorded on a PANalytical X'Pert Pro diffractometer in a Bragg–Brentano geometry ($\theta - 2\theta$), using Ge(1 1 1) monochromated Cu Kα1 radiation (λ = 1.54051 Å). For the determination of the low-temperature structure of $Rb_2KCr(Ga)F_6$, X-ray diffraction data were collected for a small single crystal using an Xcalibur (Oxford Diffraction) diffractometer with CCD area detector, with a sealed-tube MoKα X-ray source. For measurements at low temperature, an open flow cryostat (Oxford Cryosystem) was used. Integration of intensities and data reduction applied to the different data sets were performed using the CrysAlis Software Package. The program package Jana2000 was used for the numerical absorption correction and structure refinements.

2.2.2. Magnetization measurements

The magnetic properties were determined on powdered samples from 4.2 to 300 K. A vibrating sample magnetometer, Faraday microbalance and SQUID device were used. To obtain accurate values of the ordering temperatures and saturation magnetization of the ferromagnetic materials, measurements were also made at the Service National des Champs Intenses (CNRS-Grenoble, France). An extraction method was used down to 1.6 K under applied magnetic fields up to 15 T.

2.2.3. Electrical conductivity

For conductivity measurements at ambient pressure, the compound was compressed to a cylindrical pellet. Two Cu electrodes with welded electrical wires were set on both sides. The pellet was then placed in a teflon matrix and covered with powdered teflon. The setting was pressed up to 500 bar and sintered in order to ensure a waterproof cell. With such an encapsulated sample, electrical measurements were satisfactorily performed up to 550 K. Piezoresistive properties of $M^{II}M^{IV}F_6$ compounds were studied using a belt-type unit, able to reach 90 kbar. The pressure dependence of the resistivity was followed "in situ" using a cell specially designed for the purpose by G. Demazeau at ICMCB Bordeaux. The cell was composed of a cylindrical pyrophyllite body with two teflon O-rings. In order to prevent hydrolysis, the sample was coated with AlF_3. This unit was inserted into a Pt microfurnace. An additional protective layer of La_2O_3 was set inbetween the furnace and the pyrophyllite body.

2.2.4. Calorimetric measurements

Phase transitions in elpasolites were studied at KIP, Krasnoyarsk, Russia, on a Perkin-Elmer DSC-7 differential scanning calorimeter operating down to 100 K. The compound was sealed in an aluminium sample holder. Temperatures and enthalpy were calibrated using two samples: the melting temperature of pure indium and the melting temperature of pure mercury. The temperatures were determined with an accuracy ±0.2 K and the uncertainty on the enthalpy value was estimated as ±5 J/mol. The heating and cooling rates were fixed at 5 K/min in a He gas atmosphere.

2.2.5. Surface area measurements

N_2 adsorption isotherms were obtained at 77 K using an ASAP 2000 instrument from Micromeritics. The powdered sample having a mass around 200 mg was evacuated overnight at 573 K under 0.1 Pa prior to adsorption. The specific surface area $S_{(BET)}$ was calculated from BET results applied in the P/Po (0.03–0.25) range. The estimated standard deviation (esd) has been calculated for surface areas larger than 30 $m^2 g^{-1}$ and is equal to 5 $m^2 g^{-1}$.

Table 1
Magnetic data of Pd_2F_6-type ferromagnets.

Compound	T_C (K)	M_{sat} (BM) at 4.2 K	Θ_p (K)	C_{mol}
$NiPdF_6$	6.0	1.42	4	1.32
$NiPtF_6$	8.0	1.10	4	1.31
Pd_2F_6	10.0	1.80	8	1.33
$PdPtF_6$	25.0	1.70	6	1.26
Pt_2F_6	16.0	1.60	18	1.20

2.2.6. Scanning electron microscopy

SEM pictures were obtained with a FX 600 microscope. Surface charge elimination was achieved by silver deposition.

2.2.7. Transmission electron microscopy

Transmission electron microscopy (TEM) was performed on a TECNAI F20 instrument with a field emissive gun, operating at 200 kV and with a point resolution of 0.24 nm. Fast Fourier transforms (FFT) of high resolution transmission electron microscopy (HRTEM) images were calculated using the Gatan Digital Micrograph software. TEM samples were prepared by dissolving several milligrams of powder in ethanol, before being deposited on a Formvar/carbon copper grid.

3. Ferromagnetism and piezoconductivity in Pd_2F_6 and $M^{II}M^{IV}F_6$ complex fluorides [*This topic was part of collaboration with Prof. Neil Bartlett until his early death on August 5, 2008*]

$M^{II}M^{IV}F_6$ compounds (M^{II} and/or M^{IV} are transition elements) generally derived from ReO_3- or VF_3-type structures. The arrangement corresponds to a NaCl-type packing of ($M^{II}F_{6/2}$) and ($M^{IV}F_{6/2}$) octahedra. Several structural types have been proposed depending on the presence or absence of a cationic ordering (see for instance [1]). It was previously demonstrated by neutron diffraction that so-called "PdF_3" was, in fact, Pd_2F_6, with an ordering between Pd^{II} and Pd^{IV} species [12]. The compound crystallized in the $LiSbF_6$-type (space group $R\bar{3}$). X-ray powder diffractograms have shown $NiPdF_6$, $NiPtF_6$, $PdPtF_6$ and $PdSnF_6$ to be isostructural with Pd_2F_6 [13]. Table 1 summarizes the magnetic data of Pd_2F_6-type ferromagnets. In the paramagnetic state the effective moment is due to the contribution of the M^{II} cations only, Pd^{IV} and Pt^{IV} being diamagnetic species.

All these ferromagnetic materials are characterized by a three-dimensional ordering between tetravalent cations with empty e_g orbitals (Pd^{IV} and Pt^{IV} in the low-spin $t_{2g}^6 e_g^0$ configuration) and divalent cations with a high-spin $t_{2g}^6 e_g^2$ configuration. Super-exchange couplings involving e_g electrons of the divalent cations are responsible for the ferromagnetic behaviour. One electron from the half-occupied e_g level of M^{II} is transferred, without spin changing to an empty e_g level of Pd^{IV} and Pt^{IV} via p atomic orbitals. Resulting delocalization and correlation mechanisms are both ferromagnetic.

The pressure dependence of the resistivity (ρ) of Pd_2F_6 at 25 °C, measured in situ in a solid-state high-pressure "belt" instrument, shows that the values drop by six orders of magnitude up to 80 kbar [13] (Fig. 1). The material was proposed as a pressure sensor because of the linear response of the resistivity variation over a large pressure range. The activation energy determined from the slope of the cooling cycle diminishes with applied pressure: for $P = 20$ kbar, ΔE is equal to 0.24 eV and for $P = 60$ kbar, ΔE is as low as 0.07 eV. For both types of measurements, i.e., $d\log\ \rho = f(P)$ at constant T and $d\log\rho = f(T)$ at constant P, the materials have been surveyed by X-ray diffraction after every quenching cycle. The drastic decrease in resistivity in Pd_2F_6 can be attributed to a motion of the fluoride ions towards the center of the Pd^{II}–F–Pd^{IV} bonds. Concerning the pressure dependence of the energy diagram, in addition to a decrease of the gap between Pd^{II} and Pd^{IV} e_g levels, new e_g^1 Pd^{III} levels appeared. A hopping mechanism would arise between Pd^{II} and Pd^{III} species and also between Pd^{III} and Pd^{IV}. The values of the activation energies observed at high pressures are similar to those of semiconductor oxides showing hopping properties. However, the still high value of the resistivity ($10^4\ \Omega$ cm) could be explained by a lower mobility of the localized electrons. A drastic increase in conduction was also observed when other $M^{II}M^{IV}F_6$ compounds were subjected to high pressures (Fig. 1). The importance of the transition gap seems to correlate with the extension of the participating metal orbitals. The difference between the resistivity at room pressure and under 80 kbar is of 5–6 orders of magnitude when 4d–4d orbitals (Pd_2F_6), or 3d–5d orbitals ($NiPtF_6$, $CuPtF_6$) are involved, whereas a difference of about 2 orders of magnitude is observed in the 3d–4d case ($NiPdF_6$, $CuPdF_6$). Because all these phases contain M^{II} elements with half-filled e_g orbitals and M^{IV} elements with empty e_g orbitals, an electronic transition similar to that occurring in Pd_2F_6 can be assumed.

4. Mechanisms of ferroelastic phase transitions in A_2BMF_6 elpasolites [*This topic is part of collaboration with Dr. I.N. Flerov and his group at the Kirensky Institute of Physics, Krasnoyarsk, Russia, F. Rodriguez at Universidad de Cantabria, Santander, Spain and with J. Darriet at ICMCB-CNRS*]

Numerous compounds with the general formula A_2BMX_6 (A, B = Cs, Rb, K, NH_4, Na; M = trivalent ions including rare earth

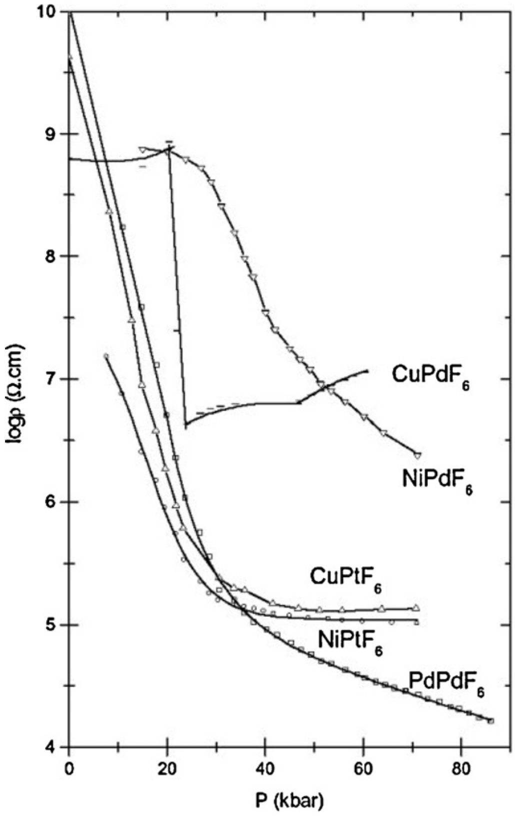

Fig. 1. Pressure dependence of resistivity for some $M^{II}M^{IV}F_6$ compounds at 25 °C.

Table 2
Transition mechanisms in Rb_2KMF_6 elpasolites.

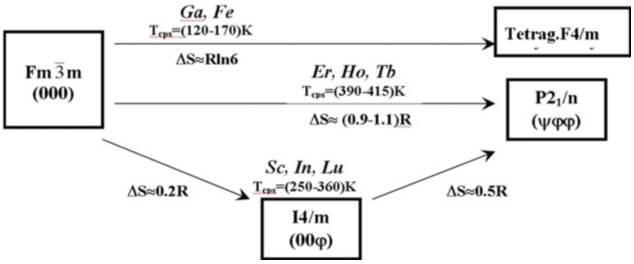

elements, X = O, F) belong to the elpasolite family with a K_2NaAlF_6 cubic prototype structure (space group Fm–3m, $a \sim 8.1$–9.5 Å, $z = 4$). The structure is derived from the AMF_3 perovskite by the presence of monovalent cations in both octahedral sites ($^{VI}B^+$), and CN = 12 sites ($^{XII}A^+$) [1]. In many of these compounds, structural phase transitions (SPT) occur in a large temperature range, depending on the value of the Goldschmidt tolerance factor t [1]. The sizes of the involved cations are decisive and considerably affect the sequence and the stability range of the low-temperature distorted phases [14]. Such a point can be illustrated by the rare-earth based Rb_2KMF_6 series [15–17]. For smaller RE ionic radii: M = Lu, Sc or In, two successive SPTs are observed from high to low temperatures: Fm–3m → I4/m → $P2_1/n$, as shown in Table 2. The stability range of the intermediate tetragonal phase decreases with increasing size of M^{3+} cation and for $r\ M^{3+} > 0.88$ Å, that is for M = Ho, Tb, only one structural transition is observed: Fm–3m → $P2_1/n$ [18]. Ferroelastic SPT occurring in these crystals can be considered as displacive ones and are relative to small octahedral tilts around one (two or three) of the four-fold axes of the cubic phase. Simple rotational distortions of elpasolite structure are shown in Fig. 2 that result from octahedra tilts (0 0 φ) (a) and (0 0 ψ) (b) relative to the condensation of the components of modes τ^9 (k 1 1) – Γ_4^+ and τ^3 (k 1 0) – X_4^+, respectively. Atomic displacements during the phase transition to the Fm $\bar{3}$ m space group are represented in Fig. 2c for the elpasolite Rb_2KYF_6. Subsequently, the total entropy could be calculated by summarizing the entropies of the successive tilts [15].

Photoluminescence of Cr^{3+}-doped Rb_2KGaF_6 and its dependence on the local structure around Cr^{3+} have shown that structural correlations could be raised between the crystal-field parameter 10Dq and the Cr–F distance, R_{Cr-F}. High-pressure experiments performed on Rb_2KCrF_6 indicated that the excited-state spin crossover, $^2E_g(G) \leftrightarrow {}^4T_{2g}(F)$ takes place around 7 GPa with a change in luminescence from a broad band to a narrow line emission. The results point out the suitability of selecting A_2BMF_6: Cr^{3+} elpasolites to establish structural correlations between photoluminescence and R_{Cr-F} distances [19]. For smaller M^{3+} ions, such as Cr, Fe, or Ga, a different type of SPT occurs at low temperatures (LT), that is at 153, 170, and 123 K, respectively, with rather large value of the entropy change. The crystal structures of the low-temperature forms have been solved by J. Darriet et al. by single crystal X-ray diffraction [20]; the symmetry is tetragonal with F4/m space group. The cubic-to-tetragonal phase transition does not involve change in the cationic repartition. The main originality of the LT structure concerns the environment of 4/5 of the potassium atoms (in the B sublattice) which are transformed from octahedral (at room temperature) into pentagonal bipyramids sharing edges with adjacent MF_6 octahedra containing Cr or Ga. The SPT can be simply explained by the rotation of 45° in the (a,b) plane of 1/5 of the MF_6 (M = Cr, Ga) octahedra, as shown in Fig. 3. This structural model does not belong to any known distortion mechanism in double perovskite because the proposed rotational mechanism is purely localized and not cooperative, as required in the Glazer's classification [21]. The similarity between this phase transition and the transformation of perovskite into tetragonal tungsten bronze (TTB) has been raised, as shown in Fig. 4: TTB network can be derived from a A-cationic deficient perovskite structure (AMO_3) by cylindrical rotation faults, i.e. by rotation of a square group of four corner-sharing octahedra through 45° [22].

5. Nanosized $M(OH, F)_3$ aluminium hydroxyfluorides: correlations between structural features, thermal stability and acidic properties [*This work was initiated at ICMCB-CNRS by Dr. Alain Demourgues and constitutes the body of D. Dambournet PhD thesis*]

In the first two examples, the average size of the particles was micrometrical or over, since the materials were prepared mostly using conventional solid state syntheses. For other types of applications or properties, a much lower particle size is required for the materials to be useful, for instance for catalytic reactions.

Numerous inorganic materials used as acidic heterogeneous catalysts in organic reactions such as alkylation and acylation of aromatic compounds, polymerization, halogen exchange are oxides. The number and strength of Brønsted/Lewis acid sites and the specific area of the materials can often be considered as key factors for their activities. The incorporation of a more electronegative anion such as F^- is known to increase the activity by enhancing the acidic properties of the catalyst [23–25]. Previous

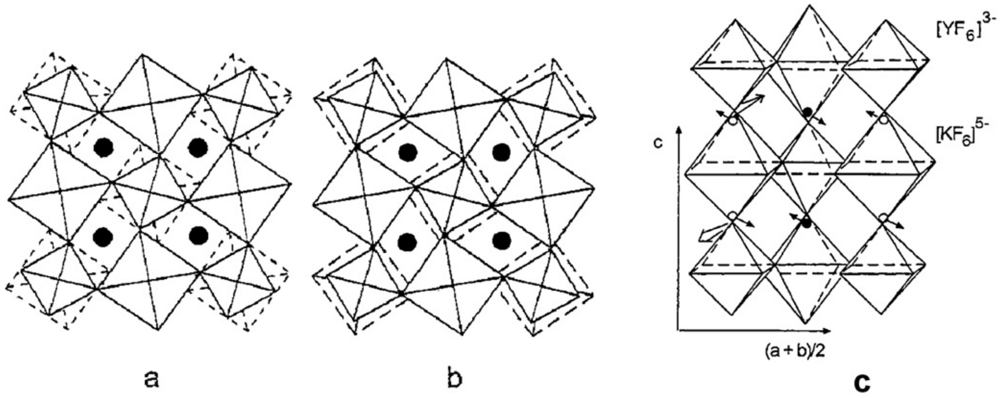

Fig. 2. Simple rotational distortions of the elpasolite structure as a result of octahedra tilts (0 0 φ) (a) and (0 0 ψ) (b). Projection along the [1 1 0] direction of elpasolite Rb_2KYF_6 (c). [Arrows schematize atomic displacements during the phase transition to the Fm $\bar{3}$m space group ($a = 9.322$ Å at 420 K). Atomic positions: Y^{3+} (4a) 0, 0, 0; K^+ (4b) 1/2, 1/2; Rb^+ (8c) 1/4, 1/4, 1/4; F^- (24e) x, 0, 0 ($x \sim 0.2$)] (see Ref. [15]).

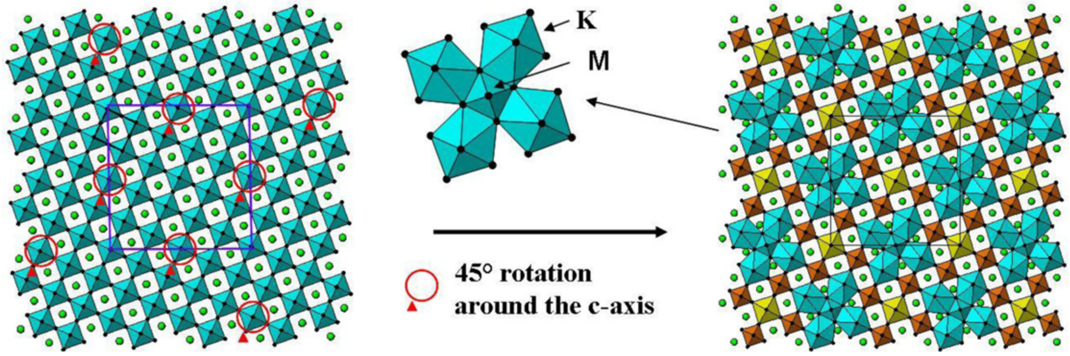

Fig. 3. Low-temperature form of Rb_2KMF_6 with M = Cr, Ga (from Ref. [20]).

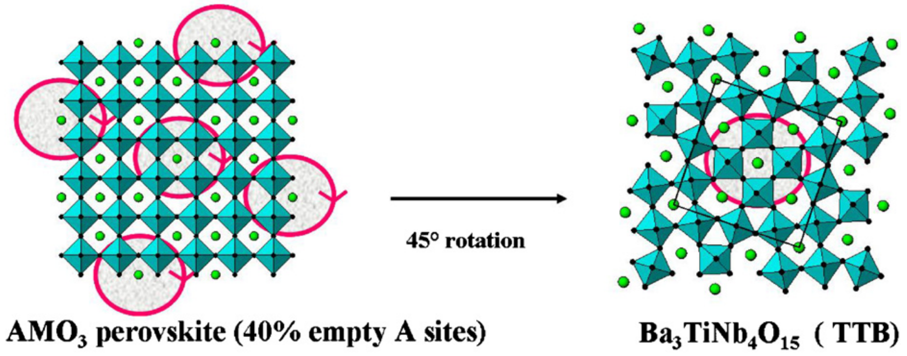

Fig. 4. Transition mechanism of AMO_3 perovskite into tetragonal tungsten bronze (TTB) (from Ref. [20]).

Table 3
Optimized reaction conditions (precursors, solvents, solvothermal parameters) for obtaining the three Al hydroxyfluoride varieties.

Final compound	Al^{3+} precursor	Solvents	HF/Al molar ratio	Temperature of solvothermal reaction (°C)	Duration time	Outgassing temperature (°C)
Pyrochlore	Isopropoxide	Isopropanol H_2O, ether	2.1	160	1 h	300
HTB	Nitrate	Isopropanol H_2O	3	160	2 h	300
ReO_3 derived	Chloride	Isopropanol H_2O	3.5	170	1 h	350

work related to inorganic fluorides, in particular Al-based ones, demonstrated that the networks may exhibit fluorinated open framework and consequently well defined cleavage planes, possessing good catalytic activity in particular in the case of the synthesis of CFC alternatives.

Microwave-assisted technique has been shown to be suitable for the achievement of high surface area metal-based fluorides, following in particular the PhD thesis works of Dambournet [26]. Depending on the chosen experimental conditions, three different structural networks can be stabilized in the Al–F–OH system: pyrochlore, hexagonal tungsten bronze (HTB) or ReO_3-derived. It can be noted that such structural types were discovered some decades ago in A_xMF_3 systems (M = d-transition metal) [27–29]. Among the various parameters that can be tuned during the experiments (see Section 2), one of most decisive is the [HF]/[Al] precursor molar ratio. When this ratio is about 2, a pyrochlore variety of aluminium hydroxyfluoride can be stabilized, whereas higher molar ratios lead to the synthesis of HTB and distorted-ReO_3 forms [26,30]. The dominant effects of the different parameters are illustrated in Table 3 where the optimal conditions are grouped to obtain either the pyrochlore, the HTB, or the ReO_3-derived form.

Table 4
Dependence of the final surface area of the pyrochlore Al hydroxyfluoride on the type of precursor and solvents (HF/Al molar ratio ~2; solvothermal reaction at 160 °C, 1 h).

Al^{3+} precursor	Types of solvents and volume ratio	Surface area ($m^2\,g^{-1}$)
Nitrate	Isopropanol/water: 1/1	6
Isopropoxyde	Isopropanol/water: 1/1	77
Isopropoxyde	Isopropanol/water/ether: 1/1/0.3	137

For HSA aluminium hydroxyfluoride with the pyrochlore-type structure, the optimization of the crystallite size and surface area of the material has been performed by varying several synthetic parameters [31]. The drastic influence of the type of precursor and solvents on the final surface area of the pyrochlore Al hydroxyfluoride (solvothermal reaction at 160 °C over 1 h, with a HF/Al molar ratio ~2) is indicated in Table 4. The final compound is formed from nanosized particles with an average particle size of 12 nm, as calculated by XRD, and confirmed by TEM observations, leading to a surface area around 140 $m^2\,g^{-1}$. HRTEM micrographs of nano-particles of Al-based hydroxy-fluoride materials, with pyrochlore networks is given in Fig. 5A. ^1H, ^{19}F and ^{27}Al NMR studies provide evidence for a disorder which is correlated to the distribution of O and F atoms on the 48f crystallographic site. ^{19}F and ^{27}Al NMR spectra confirm a larger amount of hydroxyl in the pyrochlore than in HTB phases, in agreement with the proposed chemical formula: $AlF_{1.50}OH_{1.50}$. High field ^{27}Al NMR enables the quantification of the various $AlF_{6-x}(OH)_x$ environments and supports the statistical distribution of the F atoms and of the

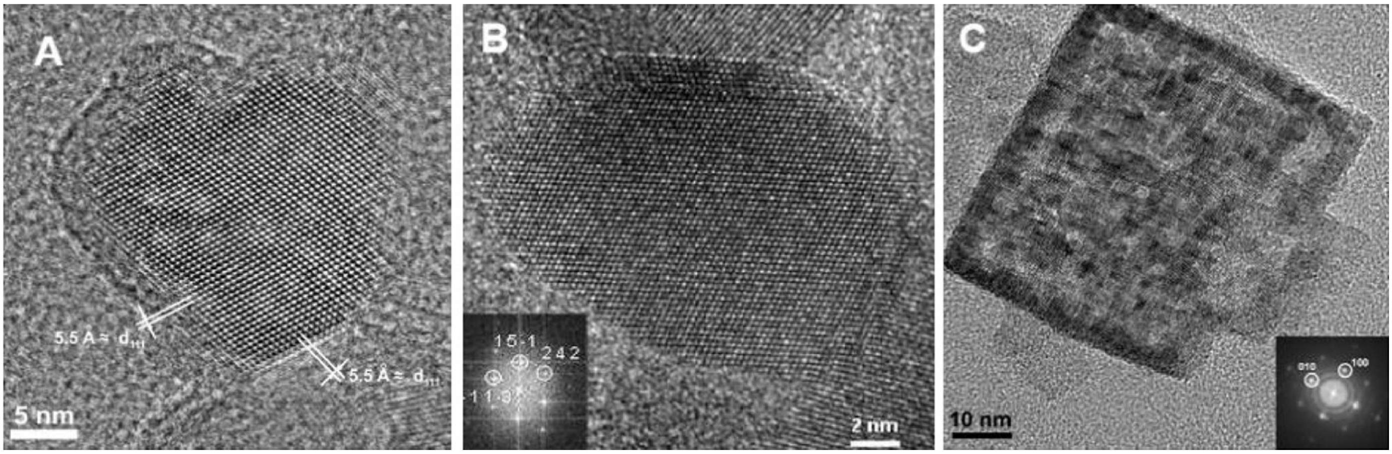

Fig. 5. HRTEM micrographs of nano-particles of Al-based hydroxy-fluoride materials: (A) pyrochlore, (B) HTB and C) ReO_3-derived forms [from Ref. [26]].

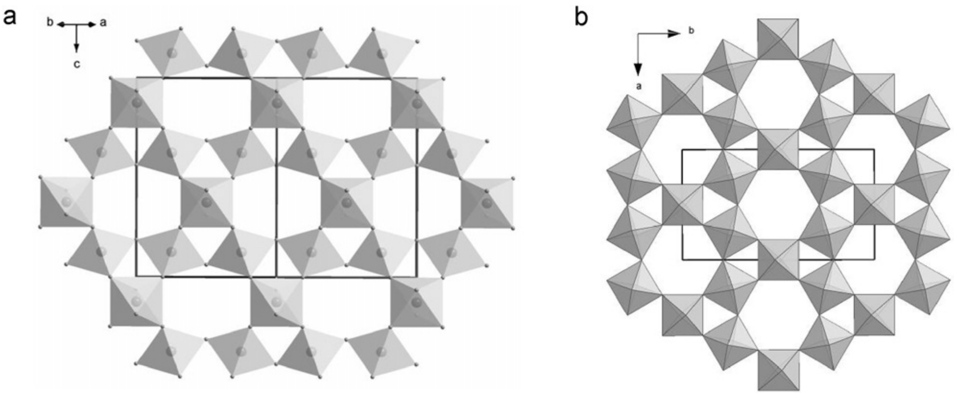

Fig. 6. The pyrochlore (a) and HTB (b) networks: view along the [1 1 0] direction and along the *c* axis.

OH groups in 48f sites. Pyrochlore and HTB network are characterized by tunnels of hexagonal section, but in the former type these tunnels are 3D connected, whereas in the latter they are oriented along the *c*-axis of the hexagonal cell (Fig. 6). FTIR and NMR have been used to get more insight into the channel environment where hydrogen bonds have been evidenced. Two different intercalated water configurations have been observed depending on the nature of the anionic environment: the water molecules being H-donor with fluoride ions and H-acceptor with hydroxyl groups in their vicinity (Fig. 7). The use of CD_3CN and pyridine as probe molecules shows that nano-hydroxyfluoride with the pyrochlore type has Lewis and Brønsted acid sites that are stronger than those of alumina, confirming the influence of fluorine content on the acid properties of AlF_3 materials. IR spectroscopy allows us to distinguish the hydroxyl groups present on the outer surface (at 3720 cm^{-1}) from those located inside the channels (at 3673 cm^{-1}). Due to steric hindrance, the latter are not accessible to the probe molecules, whereas accessible ones, present on the outer surface, generate weak and strong Brønsted acid sites.

In the case of the HTB-type compound (Fig. 6b), as far as the aluminium nitrate precursor is concerned, a secondary reaction occurring during the microwave-assisted synthesis has been identified and involves the reduction of nitrate to amine groups coupled with the oxidation of isopropanol. The surface area has also been monitored depending on the water/isopropanol volume ratio [11,26]. X-ray diffraction analysis has revealed that the anisotropic line broadening is a size effect. This behaviour has been successively solved by the introduction of a size model in the Rietveld procedure. It has been concluded from X-ray diffraction data refinements and TEM results that the crystallites possess a platelet shape with an average particle size of 15 nm associated with the high surface area of 82 m^2 g^{-1} (Fig. 5B). The occurrence of hydroxyl groups inside the network has been detected by FTIR spectroscopy. The presence of OH groups inside the HTB network seems to strongly disrupt the framework, as revealed by the difficulty to obtain accurate Al–(OH,F) distances. In the HTB hydroxyfluoride series, there is a competition between the formation of M–F and M–OH bonds, which depends on the type of M^{3+}cation, the nature of precursor and the synthetic route. It can be proposed that the ratio of linked-to-free hydroxyl groups, as well as water trapped inside the framework, which has been detected by FTIR, may explain the differences in the thermal stabilities of these solids. For instance, the comparison between Al^{3+} and Fe^{3+} hydroxyfluorides has shown that the Al–(F,OH) bond is more stable than the Fe–(F,OH) one, with a difference of more than 200 K in their thermal stability. The presence of a large amount of OH^- groups around Al^{3+} also contributes to a higher thermal stability. ^{19}F NMR as well as high-field ^{27}Al NMR have quantified the various $AlF_{6-x}(OH)_x$ environments and confirmed the preferential location of OH groups in 8f (F1) and 16 h (F2) Wyckoff positions of the HTB structure. Finally, FTIR spectroscopy

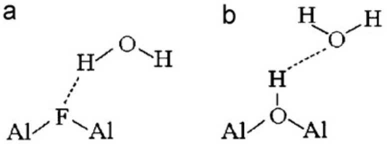

Fig. 7. Configurations of intercalated water in pyrochlore $AlF_{1.50}OH_{1.50}$.

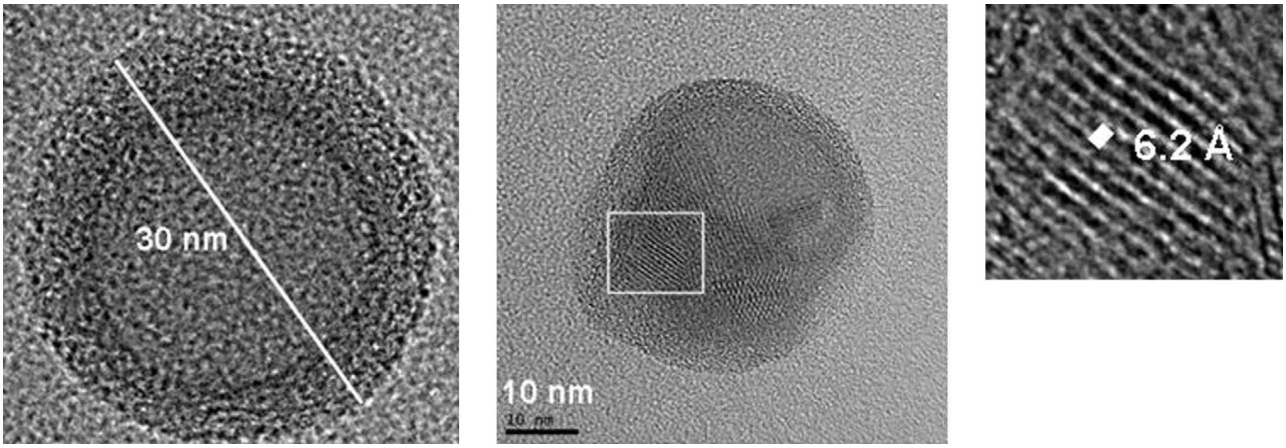

Fig. 8. HRTEM micrographs of core–shell particles of HTB-type sample annealed at 600 °C [from Ref. [26]].

has shown the presence of strong Lewis acid sites by NH_3 adsorption. The excellent acidic properties of nanosized β-$AlF_{3-x}(OH)_x$ have also been evaluated by adsorption of other probe molecules: pyridine, CO, ^{36}Cl radiotracers [32].

It should be noted that even larger surface areas can be attained by microwave heating non aqueous sol–gel fluorides prepared by E. Kemnitz at Humboldt University, Berlin [23–25]. The final material depends on the temperature heat treatment used. Three types of materials can be obtained: (i) for low temperature heat treatment, i.e., 90 °C, X-ray amorphous alkoxy-fluoride, (ii) for the highest temperature used, i.e, 200 °C, HTB form (β-AlF_3), with a surface area of 125 $m^2\,g^{-1}$ [33], (iii) finally, at an intermediate temperature, i.e., 180 °C, a multi-component material mixture exhibiting a surface area as high as 525 $m^2\,g^{-1}$. In order to remove remaining organic moieties, while retaining HSA characteristics, a post-treatment by mild fluorination was performed using F_2-gas at 225 °C. The resulting Al-based fluorides still possess a high surface area of 330 $m^2\,g^{-1}$. This new HSA material exhibits strong Lewis acidity as revealed by pyridine adsorption and catalytic tests. It has been shown that whatever the composition/structure of the Al-based fluorides materials, the number of strong Lewis acid sites is related to the surface area, highlighting the role of surface reconstruction occurring at the nanoscopic scale on the formation of the strongest Lewis acid sites [33].

Concerning the thermal behaviour of β-type aluminium hydroxyfluoride, the HTB-type network appears to be stable up to 600 °C. During the annealing treatment, dehydroxylation and pyrohydrolysis reactions occur [34]. Such an equilibrium leads to an almost complete transformation of the outermost surface of the nanoparticles, yielding a core–shell like morphology, as shown in Fig. 8. The core has been identified as β-AlF_3 by XRD and NMR. The outer most region appears X-ray amorphous, mostly constituted of oxygenated species and is built of aluminium in octahedral and under-coordinated environments, i.e., AlX_4 and AlX_5, as detected by NMR. The shell was assumed to display a spinel-like network which ensures the stabilization of observed four and five-fold coordinated Al^{3+}. The newly formed surface exhibits a lower Lewis acidity than β-$AlF_{2.6}(OH)_{0.4}$; however, strong Brønsted acid sites are still present, as revealed by pyridine adsorption [34].

The third structural type, obtained for an [HF]/[Al] ratio larger than 3, derives from the ReO_3 type structure, i.e., the high temperature structure of α-AlF_3. The cubic symmetry of the structure was confirmed by the Fast Fourier Transforms (FFT) of the HRTEM images displayed on Fig. 5C (inset). It can be noteworthy that the cubic symmetry is additionally reflected by the shape of the nano-structured particles. The acidification by higher HF contents favors the stabilization of water molecules in the first coordination spheres of the cations, as opposed to OH groups which are mostly present in pyrochlore or HTB compounds. The cubic symmetry adopted by this compound is due to the presence of water molecules, surrounding Al^{3+} cations, which induces cationic vacancies as revealed by Rietveld refinement (Fig. 9). The following chemical formula $Al_{0.82}\square_{0.18}F_{2.46}(H_2O)_{0.54}$ is supported by chemical analyses and TGA measurements [35]. The

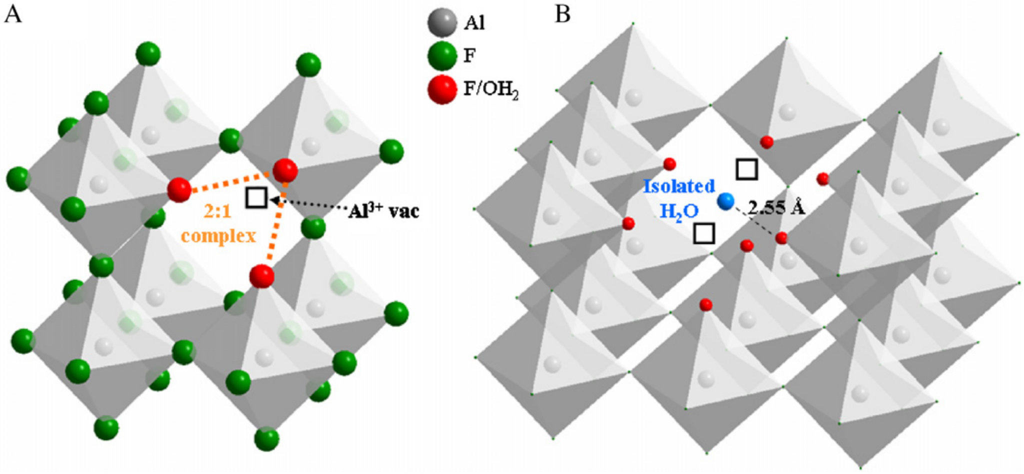

Fig. 9. Schematic representation of the ReO_3-derived structure: Al^{3+} vacancy with a 2:1 complex (A); occurrence of two vacancies with an isolated water molecule in between (B) [from Ref. [26]].

Table 5
Structural characteristics of HSA Al hydroxy-fluorides.

Structure type	Composition	Symmetry	Unit cell (Å)	Distances and angles
ReO_3-derived	$Al_{0.82}\square_{0.18}F_{2.46}(H_2O)_{0.54}$	Cubic, Pm–3m, $Z = 1$	$a = 3.6067(1)$	Al–F: 1.8034(1) Å F–F: 2.5503(1) Å
HTB	$AlF_{2.6}(OH)_{0.4}$	Orthorhombic, Cmcm, $Z = 12$	$a = 6.9681(2)$ $b = 12.0360(3)$ $c = 7.1434(1)$	1.77(3) < Al–(F,O) < 1.86(1) Å 140 < Al–(F,O)–Al < 173°
Pyrochlore	$AlF_{1.8}(OH)_{1.2}\cdot \varepsilon H_2O$	Cubic, Fd–3m, $Z = 1$	$a = 9.7309(1)$	Al–(O,F): 1.824(1) Å Al–F–Al: 141.12(6)°

structural data of the three varieties are grouped in Table 5. High-field ^{27}Al NMR spectroscopy enabled identification and quantification of the following species: AlF_6 and $AlF_{6-x}(H_2O)_x$ with $x = 1$, 2, 3 and showed that vacancies are mainly surrounded by water molecules, but also by a low content of fluoride ions, as also evidenced by ^{19}F NMR spectroscopy. The hydrogen bonding network, which occurs in the vicinity of the cationic vacancies, was characterized by FTIR and ^1H NMR. A 2:1 complex: $X\cdots H–O–H\cdots X$ where X is a proton acceptor, which is related to a shift of $\nu_{sym}(OH)$ and $\nu_{asym}(OH)$, was detected. This complex appears to be stable up to 500 °C. The phase transition to the rhombohedral form occurs at around 300 °C, but at such a temperature, a large quantity of water molecules associated with cationic vacancies still remain thanks to the 2:1 complex. The acidic properties have been revealed by pyridine and CO probe molecules. At 300 °C, the solid exhibits both strong Lewis and Brønsted acidities with an equivalent number of sites providing bifunctionality. The strong acidic behaviour highlights the effect of water molecules/cationic vacancies on the surface structure. Whereas the Lewis acid strength progressively decreases with dehydration, the Brønsted acidity remains strong even at 500 °C.

Finally, the acidic characters of these solids, evaluated by FTIR analysis using probe molecule adsorption, led to the conclusion that the strongest Lewis acidity is found in homologous Al^{3+} and Ga^{3+} compounds. These characteristics can be directly related to the strengths of the M–(F,OH) chemical bonds and to the thermal stabilities of these solids. The use of the ratio χ/r^2 (χ, electronegativity and r, ionic radius), which can be assigned to an electrical field gradient around the cation, has been proposed to explain some important trends in this series. This parameter allows a more accurate approach to both the acid strength and the thermal stability and accounts for the experimentally observed sequence, which is not the case when either the ionic radius or cation electronegativity is considered separately.

6. Conclusions

Two important points should be underlined:

(i) The knowledge of accurate structural information for inorganic fluoro-compounds allows a much deeper understanding of the electronic phenomena which are at the basis of most types of physical behaviour. The dependence and stabilities of these networks with temperature allow to better approach of the stresses present in the structure and account for the observed transformations.

(ii) The significance of nanosized materials in terms of original properties is also illustrated in the fluoride-based series. In addition to the necessity for applying new synthetic routes, it clearly shows that characterization methods also require new tools because surface groups present on these HSA materials often correspond to the major species, and are accountable for the outstanding behaviour of these materials, on both chemical and physical grounds.

This dual aspect could have also been illustrated by other examples taken in recent investigations, for instance those which are carried out at ICMCB-CNRS by Alain Demourgues and co-workers, such as the discovery of new classes of colored pigments or UV absorbers in rare earth (oxy)fluorosulfides [36–38], or the synthesis of new structural types of d-transition metal (hydroxy)fluorides, (with M = Ti, Cr, Fe) with nanosized particles and high surface areas, that could be used for various purposes, in particular in Li-ion batteries [39,40].

Acknowledgements

The author is indebted to Paul Hagenmuller and Neil Bartlett for their constant interest and support of his works since the very beginning. A. Demourgues, E. Durand, D. Dambournet, L. Francke, D. Pauwels, N. Penin, members of the ICMCB Fluorine Group, are deeply acknowledged for their strong and fruitful involvement in these studies, C. Labrugère for XPS data, M. Daturi for IR spectroscopy, and my "old chap" colleague J. Darriet for brilliant structural determinations. The author is particularly grateful to Alain Demourgues and Etienne Durand for following up the tradition of high-level solid state fluorine chemistry in Bordeaux. Concerning the topics presented in this paper, cooperative programs have been carried out with Neil Bartlett from the seventies until his death in 2008, with Igor N. Flerov and the late Kirill S. Aleksandrov (1931-2010) (KIP, Krasnoyarsk, Russia) and also with E. Kemnitz (Humboldt University, Berlin, Germany), B.Žemva (IJS, Ljubljana, Slovenia), J. Winfield (Glasgow Univ., UK) in the scope of Funfluos European program.

References

[1] D. Babel, A. Tressaud, in: P. Hagenmuller (Ed.), Inorganic Solid Fluorides, Academic Press, New York, 1985, pp. 77–203 (chapter 3).
[2] C. Cardinaud, A. Tressaud, in: T. Nakajima, B. Zemva, A. Tressaud (Eds.), Advanced Inorganic Fluorides, Elsevier, 2000, pp. 437–492 (chapter 14).
[3] A. Tressaud, C. Labrugère, E. Durand, C. Brigouleix, H. Andriessen, Sci. China Ser. E-Technol. Sci. 52 (2009) 104–110.
[4] E. Lataste, A. Demourgues, H. Leclerc, J.-M. Goupil, A. Vimont, E. Durand, C. Labrugère, H. Benalla, A. Tressaud, J. Phys. Chem. C 112 (2008) 10943–10951.
[5] L.P. Demyanova, A. Tressaud, J.Y. Buzare, C. Martineau, C. Legein, Yu.N. Malovitsky, V.S. Rimkevich, Inorg. Mater. 45 (2009) 151–156.
[6] (a) H. Groult, F. Lantelme, I. Crassous, C. Labrugère, A. Tressaud, C. Belhomme, A. Colisson, B. Morel, J. Electrochem. Soc. 158 (2007) C331–C338;
(b) T. Nakajima, S. Shibata, K. Naga, Y. Ohzawa, A. Tressaud, E. Durand, H. Groult, F. Warmont, J. Power Sources 168 (2007) 265–271.
[7] (a) A.P. Kharitonov, L.N. Kharitonova, R. Taege, G. Ferrier, E. Durand, A. Tressaud, L'Actualité Chimique 301–302 (2006) 130–134;
(b) A. Tressaud, E. Durand, C. Labrugère, in: R. d'Agostino, P. Favia (Eds.), Plasma Processes & Polymers, Wiley-VCH, 2005.
[8] A. Tressaud, B. Chevalier, L. Piraux, M. Cassart, J. Fluor. Chem. 72 (1995) 165–170.
[9] B. Chevalier, A. Tressaud, B. Lepine, K. Amine, J.M. Dance, L. Lozano, E. Hickey, J. Etourneau, Physica C 167 (1990) 97–101.
[10] J. Grannec, L. Lozano, in: P. Hagenmuller (Ed.), Inorganic Solid Fluorides, Academic Press, New York, 1985, pp. 17–76 (chapter 3).
[11] D. Dambournet, A. Demourgues, C. Martineau, S. Pechev, J. Lhoste, J. Majimel, A. Vimont, J.C. Lavalley, C. Legein, J.Y. Buzaré, F. Fayon, A. Tressaud, Chem. Mater. 20 (2008) 1459–1469.
[12] A. Tressaud, M. Wintenberger, N. Bartlett, P. Hagenmuller, C.R. Acad. Sci. 282 (1976) 1069–1072.
[13] A. Tressaud, N. Bartlett, J. Solid State Chem. 162 (2001) 333–340.

[14] I.N. Flerov, M.V. Gorev, A. Tressaud, N.M. Laptash, Crystallogr. Rep. 56 (2011) 9–17.
[15] I.N. Flerov, M.V. Gorev, K.S. Aleksandrov, A. Tressaud, J. Grannec, M. Couzi, Mater. Sci. Engin. R24 (1998) 81–151.
[16] I.N. Flerov, A. Tressaud, K.S. Aleksandrov, M. Couzi, M.V. Gorev, J. Grannec, S.V. Melkinova, J.P. Chaminade, S.V. Misyul, V.N. Voronov, Ferroelectrics 124 (1991) 309–314.
[17] I.N. Flerov, M. Gorev, W. Bürher, P. Böni, A. Tressaud, J. Grannec, Physica B (Amsterdam) 234–236 (1997) 144–145.
[18] I.N. Flerov, M.V. Gorev, J. Grannec, A. Tressaud, J. Fluorine Chem. 116 (2002) 9–14.
[19] I. Hernández, F. Rodríguez, A. Tressaud, Inorg. Chem. 47 (2008) 10288–10298.
[20] F.J. Zúñiga, A. Tressaud, J. Darriet, J. Solid State Chem. 179 (2006) 3607–3614.
[21] A.M. Glazer, Acta Crystallogr. B 28 (1972) 3384–3392.
[22] B.G. Hyde, M. O'Keefe, Acta Crystallogr. A 29 (1973) 243–248.
[23] E. Kemnitz, D.H. Menz, Prog. Solid State Chem. 26 (1998) 97–153.
[24] E. Kemnitz, U. Gross, S. Rudiger, C.S. Shekar, Angew. Chem., Int. Ed. 42 (2003) 4251–4254.
[25] E. Kemnitz, U. Gross, St. Rüdiger, G. Scholz, D. Heidemann, S.I. Troyanov, I.V. Morosov, M.-H. Lemée-Cailleau, Solid State Sci. 8 (2006) 1443–1452.
[26] D. Dambournet, Ph.D. Thesis, University Bordeaux1, January 2008.
[27] R. de Pape, C.R. Acad. Sci. 260 (1965) 4527–4530.
[28] R. de Pape, A. Tressaud, J. Portier, Mater. Res. Bull. 3 (1968) 753–758.
[29] M. Leblanc, G. Férey, P. Chevallier, Y. Calage, R. De Pape, J. Solid State Chem. 47 (1983) 53–58.
[30] L. Francke, E. Durand, A. Demourgues, A. Vimont, M. Daturi, A. Tressaud, J. Mater. Chem. 13 (2003) 2330–2340.
[31] D. Dambournet, A. Demourgues, C. Martineau, E. Durand, J. Majimel, A. Vimont, H. Leclerc, J.C. Lavalley, M. Daturi, C. Legein, J.Y. Buzaré, F. Fayon, A. Tressaud, J. Mater. Chem. 18 (2008) 2483–2492.
[32] D. Dambournet, H. Leclerc, A. Vimont, J.-C. Lavalley, M. Nickkho-Amiry, M. Daturi, J.M. Winfield, Phys. Chem. Chem. Phys. 11 (2009) 1369–1379.
[33] D. Dambournet, G. Eltanamy, A. Vimont, J.C. Lavalley, J.M. Goupil, A. Demourgues, E. Durand, J. Majimel, S. Rudiger, E. Kemnitz, J.M. Winfield, A. Tressaud, Chem. Eur. J. 14 (2008) 6205–6212.
[34] D. Dambournet, A. Demourgues, C. Martineau, J. Majimel, M. Feist, C. Legein, J.Y. Buzaré, F. Fayon, A. Tressaud, J. Phys. Chem. C 112 (2008) 12374–12380.
[35] D. Dambournet, A. Demourgues, C. Martineau, E. Durand, J. Majimel, C. Legein, J.Y. Buzare, F. Fayon, A. Vimont, H. Leclerc, A. Tressaud, Chem. Mater. 20 (22) (2008) 7095–7106.
[36] D. Pauwels, A. Demourgues, H. Laronze, P. Gravereau, F. Guillen, O. Isnard, A. Tressaud, Solid State Sci. 4 (2002) 1471–1479.
[37] F. Goubin, X. Rocquefelte, D. Pauwels, A. Tressaud, A. Demourgues, S. Jobic, Y. Montardi, J. Solid State Chem. 177 (2004) 2833–2840.
[38] D. Pauwels, F. Weill, A. Tressaud, A. Demourgues, Chem. Mater. 18 (2006) 6121–6131.
[39] N. Penin, N. Viadere, D. Dambournet, A. Tressaud, A. Demourgues, in: Proceedings MRS Fall Meeting, Boston, USA, November, 2005.
[40] A. Demourgues, N. Penin, E. Durand, F. Weill, D. Dambournet, N. Viadere, A. Tressaud, Chem. Mater. 21 (2009) 1275–1283.